The dust environment of comet 29P/Schwassmann-Wachmann 1 from dust tail modeling of 2004 near-perihelion observations

F. Moreno

Instituto de Astrofísica de Andalucía, CSIC, PO Box 3004, 18008 Granada, Spain

fernando@iaa.es

ABSTRACT

A Monte Carlo inverse dust tail modeling of ground-based images of comet 29P/Schwasssmann-Wachmann 1 has been performed. The images of the comet were acquired on several nights on July 2004, a few days after the 2004 perihelion passage. The analysis takes into account the rotation properties of the comet, incorporating dust ejection from active areas on the nucleus surface. We demonstrate that these models provide a significant improvement over models having a fixed sunward hemispherical particle emission cone, owing to the observed coma asymmetry, giving excellent fits to the observed intensity isophote fields. The rotation parameters, defined by the argument of the subsolar meridian at perihelion, Φ, and the obliquity, I, are found to be compatible with those derived by Sekanina (1990) from morphological studies (Φ=279°, and I=100°). We found that if dust emission is assumed to be produced by a single active area driven by insolation, this must be then located on the southern hemisphere near –35° latitude. We have devised a method to impose $Af\rho(t)$ constraints over the overdetermined system of equations leading to the solution of the dust mass loss rates and size distribution function. When those constraints are applied, the time-averaged particle size distribution function was found to be characterized by a power law of index in the range –3.7 to –3.3, and a dust loss mass rate approximately in the nominal range of 300 to 900 kg s^{-1}, depending on different model approaches, and for an albedo times the phase function of 0.1, confirming the fact that this comet as perhaps the most active source of interplanetary dust, providing some 3-10% of the mass required to replenish the losses of the interplanetary dust cloud if it is in steady state.

Subject headings: comets: general — comets: individual(29P/Schwassmann-Wachmann 1) — methods: data analysis

1. Introduction

Periodic comet 29P/Schwassmann-Wachmann 1, with an eccentricity e=0.044, semimajor axis a=5.99 AU, and a slight inclination to ecliptic of 9.4°, moves along a nearly circular orbit just beyond Jupiter's, so it is also considered a Centaur object. This comet is well known for its episodic outbursts, which tend to recur at an average rate of a few per year (e.g. Sekanina (1990), and references therein). The comet has been sometimes reported to increase its brightness to about 6 magnitudes during outburst times, decreasing its activity in quiescent periods being described as an almost stellar object (Roemer 1958), although Jewitt (1990) observed the comet during 1987 and 1988 and always detected the presence of a coma. The detection of emission from carbon monoxide at submillimiter wavelengths by Senay and Jewitt (1994) has led to think on this gas as the primary driver of its coma activity (e.g. Senay and Jewitt (1994), Festou et al. (2001), Gunnarsson et al. (2002)). Drag forces from CO sublimation can act on icy water dust grains and push them out into the coma (e.g. Mukai (1986)). CO has been found to be released from both the Sun-facing side and the nightside of the nucleus (Festou et al. 2001), although an additional extended source coming from CO-bearing particles has also been proposed (Gunnarsson et al. (2002), Gunnarsson (2003)) based on the spatial distribution of the strength of the rotational J=2-1 line at 230 GHz.

The nucleus of 29P has an unusually large, but with somewhat uncertain size, the present estimates of the radius ranging from 27±5 km by Stansberry et al. (2004) to 15.4±0.2 km (for a geometric albedo p=0.04) or 8.6±0.1 km (for p=0.13) by Meech et al. (1993).

The dust emission pattern from 29P has been inferred from analysis of images acquired through red-sensitive photographic IIIa-F plates (Sekanina 1990), CCD photometry and imaging (Jewitt 1990), and dust tail analysis (Fulle 1992), among others. The analysis by Sekanina (1990) was made by a morphological fit to 29P images during an outburst by assuming a discrete emission source at ∼50° from the north pole. He derived the argument of subsolar meridian at perihelion, and the obliquity as Φ=279° and I=100°, respectively, and adopted a rotation period of 5 days as found by Whipple (1980). The dust tail analysis by Fulle (1992) was performed by the technique described previously in Fulle (1989), and did not include the rotational characteristics of this object. The dust mass loss rate derived by Fulle (1992), (600±300) kg s^{-1}, obtained from dust tail analysis from a single red narrow-band CCD image by Jockers et al. (1992), strongly disagrees with the loss rate derived from coma photometry by Jewitt (1990), who gave only 10 kg s^{-1}, or with the upper limit of 50 kg s^{-1} estimated by Stansberry et al. (2004).

The rotation period is another parameter which shows large discrepancies among the values reported by different authors. Thus, while Stansberry et al. (2004) gave a rotation

period of $P \geq$60 days or more, Whipple (1980) reported 4.97 days, Jewitt (1990) 6 days, and Meech et al. (1993) obtained a complex spin state with two periods near 14 and 32 hours.

In this paper, we analyze CCD imaging observations of the comet near perihelion acquired during several dates on July 2004, and perform Monte Carlo dust tail analysis incorporating the nucleus rotation parameters, in order to retrieve the dust environment that best fit the observations. In section 2 we describe the observations and reduction, while section 3 is devoted to the description of the model. Section 4 shows the results and discussion, and in section 5 reports the main conclusions of this work.

2. Observations and reduction

The observations were all performed with the 1.5-m telescope of the Sierra Nevada Observatory in Granada, Spain (MPC code J86). We used a 1024×1024 pixel CCD camera in combination with a Johnson red filter. The pixel size on the sky was $0.46''$, so that the field of view was $7.8' \times 7.8'$. Comet 29P was imaged on the nights of 23, 24, and 25 July 2004. Table 1 shows the log of the observations. The comet heliocentric distance was essentially constant at r=5.724 AU during the observations. The Earth-comet distance, phase angle, and position angle of the Sun-to-comet radius vector were $\sim$ 5.29 AU, $\sim 9.6^\circ$, and $\sim 244^\circ$, respectively. Given the pixel size and the geometry of the observations, the original spatial resolution of the images was 1765 km pixel^{-1}.

The individual images of 29P were acquired using differential guiding, with integration times in the range 400-900 sec. Flat field images were acquired from twilight exposures. The 29P images were bias subtracted and flat-fielded using standard techniques. The astrometric and photometric reductions were made using Herbert Raab's ASTROMETRICA shareware (see http://www.astrometrica.at), using the USNO-B1.0 star catalog (Monet et al. 2003). The catalog provides a 0.3 mag photometric accuracy and a $0.2''$ astrometric accuracy. Typically, 40-50 stars appearing in the CCD field of view of each image were selected for photometry (see Table 1).

The individual images were calibrated to mag arcsec^{-2}, and then converted to solar disk intensity units (denoted as sdu hereafter). Once calibrated, the images corresponding to each single night were shifted as to have the comet optocenter on the same pixel coordinates in all the images, and then the median of those images was taken. The resulting images are displayed in Figure 1. As it is seen, the images are morphologically similar among them. For modeling purposes, the images displayed in Figure 1 were rebinned by 16×16 pixels

and rotated to the (M, N) photographic plane (Finson and Probstein 1968), so that the resolution of the images for modeling was 28240 km pixel^{-1}. The images used for modeling (e.g.. those displayed in the upper panels of Figure 3) were a subset of 30×30, with the comet optocenter on pixel (16,16), so that they cover a squared region of 8.47×10^5 km in side.

We also measured the Johnson red magnitude of the 29P coma on each individual full-resolution image by using a 10-pixel (4.6″, or 8119 km on the comet images) circular aperture radius centered on the comet optocenter (Table 1). No systematic variations in the light curve that could be attributable to a modulation by the nucleus rotation was found during the three days of observations (see Figure 2). There is a relatively higher dispersion in the data for the night of July 24th, that might explain why the resulting median image was of a significant higher intensity than those of July 23th and 25th (Figure 1), which display very similar isophote fields.

3. The Model

We modeled the images by the Monte Carlo dust tail analysis, considering both a classical model in which particle ejection is assumed to occur through an emission cone with symmetry axis oriented toward the Sun, covering a solid angle of 2π, i.e., hemispherical ejection, and a rotating nucleus model, with discrete active areas on the surface. The former model will be referred to as the hemispherical emission model for short. In order to keep the number of parameters to a minimum, we have not considered opening angles different from 2π. This is justified because, as stated by Fulle (2004) on his inverse dust tail modeling on many comets, in most cases the accuracy of the fits of the observed tail brightness did not change after varying the assumed dust ejection anisotropy.

We followed the theory and formalism of the Monte Carlo approach as described in, e.g., Fulle (1989). The numerical model has been improved as to include the effects of nucleus rotation on the coma brightness distribution. A similar approach was incorporated by Fulle (1994) in his analysis of 2060 Chiron images. Our model also benefits from studies of the 29P morphology performed by Sekanina (1990). On the basis of comparisons of observed and modeled images, Sekanina (1990) concluded that the dust ejection pattern from comet 29P could be characterized by the existence of a single active area located ∼50° from the comet north rotation pole, being the values of the two nucleus spin parameters, the obliquity I, and the argument of the subsolar meridian at perihelion, Φ, of 100° and 279°, respectively. In our models, we considered a sample of $N_t N_\mu N_s$ dust grains, where N_t is the number of samples in the time interval of dust ejection, which is defined by starting and ending times

denoted by τ_1 and τ_2 (τ_1 being normally 0), N_μ is the number of samples in size, and N_s is the number of grains of a given size ejected at time t either inside the fixed emission cone in the hemispherical ejection version of the model, or from an active area defined by some cometocentric latitude and longitude domain in the rotating nucleus model. For this application, we set $N_t = N_\mu = N_s = 200$. The nucleus is considered spherical, and the dust emission is assumed to be radial. Dust emission is assumed to occur only when the active area is illuminated by the Sun.

The ejection velocity of the dust grains was assumed to be given by:

$$v_{eject}^{-1} = C^{-1}(A + B(1-\mu)^{-1/2}), \tag{1}$$

as given by Sekanina (1990) in his analysis of images of 29P, where A and B are constants whose numerical values are 1.2 and 10, respectively, when v_{eject} is to be given in km s^{-1}. We have introduced an additional constant C to be determined in the fitting procedure, as described below. In order to minimize the number of free parameters in the model, no dependence with time of the ejection velocities has been included. The parameter $(1-\mu)$ is defined as the ratio of the radiation force to that of gravity, and it is given for spherical particles by (Finson and Probstein 1968):

$$(1-\mu) = C_{pr} Q_{pr} (\rho_d d)^{-1}, \tag{2}$$

where $C_{pr} = 1.191 \times 10^{-3}$ kg m^{-2}, Q_{pr} is the scattering efficiency for radiation pressure, which is $Q_{pr} \sim 1$ for large absorbing grains (Burns et al. 1979), and ρ_d is the mass density of the spherical grain of diameter d. The density will be assumed to be $\rho_d = 10^3$ kg m^{-3}. The particles are assumed to be ejected in a interval of $(1-\mu)$ characterized by endpoints $(1-\mu)_1$ and $(1-\mu)_2$.

In the rotational nucleus model, and for a given active area latitude and longitude, the direction of the ejection velocity vector is computed by the formulas given by Sekanina (1981), by setting the ejection point randomly within the selected active area. Following Sekanina (1981), a unit vector **U** in the direction of particle ejection has three components, U_r, U_t, and U_n, corresponding to the direction of the prolonged Sun-Comet radius vector, to the perpendicular to the sunward direction in the orbit plane in the sense of the comet orbital motion, and to the direction of the northern orbital pole, from which the comet is seen to orbit the Sun counterclockwise, respectively. These components are given by:

$$\begin{bmatrix} U_r \\ U_t \\ U_n \end{bmatrix} = \begin{bmatrix} \cos(\Phi+\nu) & \cos I \sin(\Phi+\nu) & \sin I \sin(\Phi+\nu) \\ -\sin(\Phi+\nu) & \cos I \cos(\Phi+\nu) & \sin I \cos(\Phi+\nu) \\ 0 & \sin I & -\cos I \end{bmatrix} \begin{bmatrix} \cos\phi \cos(\theta+\theta_0) \\ \cos\phi \sin(\theta+\theta_0) \\ \sin\phi \end{bmatrix} \quad (3)$$

where ν is the true anomaly, θ is the angular distance of the active area from the subsolar meridian, and ϕ is the active area latitude. The latitude of the subsolar point, ϕ_0, and the longitude of the subsolar meridian from the ascending node of the orbit plane on the equator, θ_0, are given by:

$$\begin{aligned} \sin\phi_0 &= \sin I \sin(\Phi+\nu) \\ \cos\phi_0 \sin\theta_0 &= \cos I \sin(\Phi+\nu) \\ \cos\phi_0 \cos\theta_0 &= \cos(\Phi+\nu) \end{aligned} \quad (4)$$

In the hemispherical ejection model, the direction of the velocity vector is given by setting randomly the vector components within the ejection cone. The orbital elements of the ejected dust particles are then calculated according to their size and velocity. The position of the particles at a given time were computed in the cometocentric coordinate system, and then projected onto the photographic plane or (M, N) system. The fit of the dust coma or tail involves the inversion of the overdetermined linear system $\mathcal{A}\mathcal{F} = \mathcal{I}$, where $\mathcal{A}$ is the kernel matrix containing the model dust tails (for the three images included in the analysis), i.e., the surface density of the sampling particles integrated over t and $(1-\mu)$, $\mathcal{F}$ is the output vector, which contains the time-dependent $(1-\mu)$ distribution, and $\mathcal{I}$ is the observed surface brightness of the image in the selected region of the (M, N) space. The method originally developed by Fulle (Fulle 1989) involves the use of regularizing constraints that are added to the system $\mathcal{A}\mathcal{F} = \mathcal{I}$, because of the ill-posed nature of the problem. The goals using those constraints are to obtain a dust mass loss rate depending on the heliocentric distance r as r^{-2}, and to derive a size distribution varying smoothly with time. In the particular case of comet 29P, which is known to have an almost circular orbit, and to experience unevenly distributed outbursts of activity, in principle we have performed the model calculations without regularizing constraints, as the use of those regularizing constraints could mask outbursts of activity that may have leave signatures on the comet images. We always did, however, impose the obvious condition of having non-zero elements in the output vector $\mathcal{F}$. The system of equations was solved by the algorithm of Bartels and Conn (1980), that allows to impose linear constraints on the solution vector, in particular the condition $\mathcal{F}_j > 0$. To obtain the coefficients of matrix $\mathcal{A}$ we used $N_\mu = 40$ linearly distributed intervals in $(1-\mu)$ and $N_t = 42$ intervals in time.

The coefficients of matrix $\mathcal{A}$ are influenced by many physical parameters. Table 2 lists the range of variation of the parameters that has been set in order to obtain such coefficients and to solve the system of equations. Obviously, the parameters that refer to the rotational characteristics of the nucleus of 29P only refer to the rotating nucleus models. The elements of matrix $\mathcal{A}$ are influenced by the starting and ending times of particle ejection, (τ_1 and τ_2), corresponding to the ejection times since last observing run, counted backward in time. The start time obviously corresponds to the observation time of last observing run, and has been fixed to τ_1=0 s. The ending time, τ_2, has been varied between 46 days and 3.2 years, which covers all possible coma or tail ages for the different combinations of $(1-\mu)$ ranges, and ejection velocities that may occur. The $(1-\mu)$ interval should be chosen so that it represents a wide range of particle sizes expected in cometary environments, so that $(1-\mu)_1$ and $(1-\mu)_2$ were set as to cover wide domains for particle size limits.

The constant C in the ejection velocity has been varied so as to admit a velocity of up to 5 times larger than the nominal values of Sekanina (1990). We have verified that for $C < 1$, the extent of the modeled comae was too small compared to the observed comae, implying a matrix $\mathcal{A}$ with many zero files, so that no solution was feasible. The remaining parameters shown in Table 2 correspond to the rotating nucleus model only, i.e. the latitude limits of the active area, and the rotation parameters, namely obliquity I, argument of the subsolar meridian at perihelion Φ, and rotation period P. The Euler angles were adopted from Sekanina (1990), and the models were initially run for three different values of the rotation period: 14 hours, 32 hours (Meech et al. 1993), and 15 days, a value which is located somewhere in between those short periods and the very long period estimate of 60 days or more by Stansberry et al. (2004).

The goodness of the fits were provided by:

$$\sigma = \sqrt{\frac{1}{N}\sum_{i=1}^{i=N}\left[\mathcal{I}_{meas}(i) - \mathcal{I}_{fit}(i)\right]^2} \tag{5}$$

where $\mathcal{I}_{meas}(i)$ are the measured solar disk intensities of the 29P images, and $\mathcal{I}_{fit}(i)$ are the fitted solar disk intensities, the sum being extended to all pixels in the three images under study, so that N=3×30×30=2700 pixels.

Once the vector $\mathcal{F}(t, 1-\mu)$ is computed, the quantity $f(t, 1-\mu)$ is calculated as:

$$f(t, 1-\mu) = \frac{\mathcal{F}(t, 1-\mu)}{\int_{(1-\mu)_1(t)}^{(1-\mu)_2(t)} \mathcal{F}(t, 1-\mu) d(1-\mu)}, \tag{6}$$

where the integration limits $(1-\mu)_1(t)$ and $(1-\mu)_2(t)$ correspond to the minimum and

maximum values of the parameter $(1-\mu)$ considered. From this quantity, the time-averaged $(1-\mu)$ distribution function, $g(1-\mu)$, is computed by the following equation:

$$g(1-\mu) = \frac{(1-\mu)^4 \int_{t_1}^{t_2} f(t,1-\mu)dt}{C_{pr}Q_{pr}\int_{t_1}^{t_2}\int_{(1-\mu)_1}^{(1-\mu)_2}(1-\mu)^2 f(t,1-\mu)d(1-\mu)dt} \tag{7}$$

For each function $g(1-\mu)$ we made a transformation to a size distribution function using equation (2), and then a fit to a power law, from which we compute the time-averaged sized distribution power index, denoted by $\langle\alpha\rangle$.

The time-dependent dust mass loss rate is given by:

$$\frac{dM}{dt} = \frac{2r^2}{3R_\odot^2}\frac{C_{pr}Q_{pr}}{A_p(\alpha)}\int_{(1-\mu)_1(t)}^{(1-\mu)_2(t)}\frac{\mathcal{F}(t,1-\mu)}{1-\mu}d(1-\mu), \tag{8}$$

where r is the comet heliocentric distance, $R_\odot$ is the solar radius, and $A_p(\alpha)$ is the dust albedo times the phase function, assumed here to be $A_p(\alpha) = 0.1$. This is actually an upper limit for A_p at the phase angle of the observations (9.6°) (Hanner and Newburn 1989). For other values of this parameter, the dust mass loss rate should be scaled accordingly. For each model, we also computed the averaged dust mass loss rate in the time interval for which the model is performed, which we denoted by $\langle\frac{dM}{dt}\rangle$.

4. Results

As stated in previous section, we started the analysis by considering a comet nucleus having a fixed emission cone pointing directly towards the Sun, with a fixed opening angle of 2π, i.e. hemispherical ejection. That is the classical Monte Carlo dust tail analysis developed by Fulle (e.g., Fulle (2004), and references therein), that we have also independently implemented and applied to various comets (e.g. Moreno et al. (2003), Moreno et al. (2004)). We run a total of 1080 models corresponding to different input parameters as shown in Table 2. For each parameter combination, the coefficients of matrix $\mathcal{A}$ are obtained, and the overdetermined system of equations $\mathcal{A}\mathcal{F}=\mathcal{I}$ is solved. Once the vector $\mathcal{F}$ is obtained, the time-varying dust mass loss rates, and size distribution functions, and the quality of the fit, as defined by parameter σ, are computed. The size distribution functions are fitted to power laws, from which the exponent is calculated from a linear fit. For hemispherical ejection models, we refer obviously to those parameters that are independent of nucleus rotation, namely the integration time range, the $(1-\mu)$ interval, and the ejection velocity constant (rows 1 to 4 in Table 2). As previously stated, we considered hemispherical emission only.

The best fit models parameters and some derived quantities are shown in Table 3. Figure 3 shows a comparison of the observed and modeled isophote fields, along with the relation of the observed to the modeled intensities, and the derived dust mass loss rates and time-varying size distribution power index, for the best fit model (#303). All the models shown in Table 3 correspond to analogous physical parameters, giving fits with equivalent quality (σ), and similar characteristics in the derived quantities. In all cases, the ejecta age is ~ 2 years or more, being characterized by a broad size distribution function with a power-law exponent of $\approx$–4 and an expansion velocity having C=3. The derived averaged mass loss rates are found to lie in the range 300±100 kg s^{-1}.

The second step was to include the effects of rotation and the presence of an active area on the 29P surface. Based on a morphological analysis of 29P images collected at various dates during an outburst, Sekanina (1990) found that the rotational parameters characterizing the nucleus, obliquity and argument of the subsolar meridian at perihelion, were 100° and 279°, respectively (Table 2). In addition, Sekanina (1990) established the presence of an active area on the nucleus surface at a latitude of $\sim$ 40°N. He also assumed a nucleus rotation period of 4.97 days in accordance with Whipple (1980). We started to compare modeled images with observed ones using this set of rotation parameters, and varying all the others parameters within the ranges and the steps shown in Table 2. The active area, if outgassing is controlled by insolation only, cannot be, however, located on the northern hemisphere, as the cometocentric latitude of the subsolar point is confined to the range –50° to –80° in the interval 600 days preperihelion to the observation epoch (see Figure 4). After some experimentation with our Monte Carlo code in forward calculation mode, we found that the active area must be located near –30° latitude (see Figure 5). As can be seen, the morphological aspect of the image generated with an active area located in the interval [–35°,–25°] is much more similar to the observed images (see, e.g., the calibrated images shown in the upper panels of Figure 3, which are referred to the (M, N) system) than the other synthetic images generated using active areas located at higher southern latitude.

Once the latitude box was fixed, we started a similar approach as we did for hemispherical ejection models, i.e., we run all models with input parameters as shown in Table 2, incorporating those related to the nucleus rotation properties. For these runs, we maintained Φ and I as indicated in Table 2 (i.e., from Sekanina (1990)) and varied the rotation period as to be 14 hours (0.58 days), 32 hours (1.33 days), or 15 days, so that the total number of rotational model runs were 1080×3=3240. The best fit parameters for rotational nucleus models are displayed in Tables 4, 5, and 6, for the three different rotation periods assumed. The quality of the fits has improved dramatically in comparison with hemispherical ejection models (see Figures 6, 7, 8, and 9). The fast time variation in the loss rates and power law indices, which mainly affect the solutions of the case P=15 days with C=5 (Figure 8), is a

result of the instabilities of the solutions of the ill-posed overdetermined system of equations without regularizing conditions. We will come back to this issue in the next section.

The best fit models for P=0.58 days correspond to ejecta ages of 460 days or longer, with average production rates in the 1000-3500 kg s^{-1} range, with C=3 corresponding generally to those models for which the production rate is lower than for models having C=5. All of those models are characterized by a size distribution function with power index of –3.1±0.2. In comparison with hemispherical ejection models, these results indicate a much higher production rate and a less steep size distribution function, with similar ejecta age. When P=1.33 days (Table 5), the best fit models always correspond to ejecta ages of 290 days, and again for models having C=5 the production rate is much higher, about $\sim$ 5500 kg s^{-1}, than for C=3, which correspond in general to values in the range 1500-2000 kg s^{-1}. Again, the power index is less steep than for hemispherical ejection models with a power index of about –3.2±0.2. Finally, for models having P=15 days (Table 6), the overall best fit models are found (although with small differences in the derived σ). In this last case, the ejecta ages are considerably reduced, with values in the 70-180 day range, and again the models having C=5 give a higher production rate (about 2000-2300 kg s^{-1}) than those having C=3, for which a much lower production rate of about 600-700 kg s^{-1} is obtained (Figure 9). The derived power law exponents characterizing the size distribution function are always in the range –3.3±0.2.

In view of the results found for the three different rotation periods initially assumed, which favor slightly the case of P=15 days over the faster rotation periods of P=0.58 and P=1.33 days, we have also made test models considering rotation periods longer than 15 days, but could not find any improvement in the derived σ values over models with shorter rotation periods. For instance, for P=60 days, the lower limit reported by Stansberry et al. (2004) from jet morphology analysis, the best solution corresponds to σ=5.3×10^{-15} sdu, which is slightly larger than the best fits for P=15 days. The best fits for P=60 days, all of them having σ $\leq$6×10^{-15} sdu, and C=3, correspond to older ejecta ages, steeper size distributions functions, and higher production rates than the derived values for P=15 days. Specifically, they are characterized by ejecta ages in the 180-700 day range, power law exponents of –3.5±0.2, and dust production rates of 1200-1700 kg s^{-1}.

5. Discussion

The models considering a rotational nucleus having rotation Euler angles as derived by Sekanina (1990) give considerable better fits than the hemispherical ejection models. This is a logical consequence of the highly asymmetric coma shown by 29P. On the other hand,

very weak constraints on the rotation period could be placed: the best fit models having a rotation period of 15 days give a σ which is only slightly better than those having faster (0.58 and 1.33 days) or slower (60 days) rotation periods.

The derived best-fit time-averaged power indices are mostly in the range –3.3±0.2, which agrees with the estimates by Fulle (1992) of –3.3±0.3, and it is otherwise typical for many comets (see e.g. Jockers (1997)). Regarding ejection velocities, most best-fit models give ejection velocities with C=3, although there are also cases with C=5, but certainly none with C=1, which would correspond to the value assumed by Sekanina (1990). The value of C=3 imply a velocity of 18.8 m s^{-1} for particles of radius 0.015 cm and density of 1 g cm^{-3}, which is in line with the corresponding velocities derived by Fulle (1992), which are located in the 10-20 m s^{-1} range. The analysis of 29P IRAS trail images by Sykes and Walker (1992) reveals ejection velocities for particle composing the trail of 4.7-5.2 m s^{-1} ($v_{aphelion}$-$v_{perihelion}$ ejection velocities), which would translate to particles of $(1-\mu)$=3×10^{-4} in our model, equivalent to a radius of 0.2 cm with density of 1 g cm^{-3}. Sykes and Walker (1992) obtained a total trail mass of 3.16×10^{14} g century^{-1}, equivalent to 100 kg s^{-1}, if the trail is composed of particles having a maximum of $(1-\mu)$=0.001. Since the trail particles could contain particles of larger sizes, and the small particle component is not present in the trail due to the effect of radiation pressure, this number must be considered as a lower limit. Fulle (1992) derived a loss rate of 600±300 kg s^{-1}, while Jewitt (1990) derived only 10 kg s^{-1}, and Stansberry et al. (2004) obtained an upper limit of 50 kg s^{-1}. Our best fit rotational nucleus models having C=3, which is consistent with the velocities derived by Fulle (1992), are mostly in the range 500-2000 kg s^{-1} (Tables 4 to 6), with no results below 500 kg s^{-1}. Our results favor the fact that 29P constitutes, by far, the largest cometary contributor to the interplanetary dust cloud, with yearly dust mass loss rates in the range [1.6-6.3]×10^{10} kg yr^{-1}, which represent [5-22]% of the ∼2.9×10^{11} kg yr^{-1} that must be replenished if the cloud is in steady state (Grün et al. 1985).

As mentioned in the previous section, the fast variation of the derived dust mass loss rates and power law indices, that are particularly remarkable in the case of P=15 days and C=5 (see Figure 8), are the result of instabilities of the ill-posed problem, and could be smoothed out by the use of appropriate regularizing conditions. However, as anticipated, the frequent outbursts that 29P experience implies that the use of regularizing conditions is not advisable. We have instead devised a method based on the behavior of $Af\rho$ (A'Hearn et al. 1984), a quantity that has been used by many authors as a proxy of the dust production rate in comets. There are some databases of $Af\rho$ measurements of 29P by astronomical amateur associations like the Italian *CARA* (Cometary Archive for Amateur Astronomers Project) and the Spanish *Cometas-Obs* which are useful for comparison with models. Fulle (2000) has shown that the quantity $Af\rho$ may be written as a function of the vector solution

$\mathcal{F}$ and the ejection velocities as:

$$Af\rho(t) = \frac{2r^2}{R_\odot^2} \int_{(1-\mu)_1(t)}^{(1-\mu)_2(t)} \frac{\mathcal{F}(t, 1-\mu)}{v(t, 1-\mu)} d(1-\mu) \tag{9}$$

The above equation, after discretization of the integral, actually provides us with a linear condition on the vector solution $\mathcal{F}$ that may be incorporated as a linear constraint when solving the system of equations $\mathcal{A}\mathcal{F}$=$\mathcal{I}$. Then, if a temporal series of measurements of $Af\rho$ is at hand, we should be able to constrain our solution vector at the time intervals those measurements are available. Figure 10 displays the measurements made from the above mentioned amateur associations in the vicinity of the 2004 perihelion and earlier. There is a general agreement between both data sets, showing the presence of evenly spaced outbursts of activity of different intensity.

There are a number of circumstances on those measurements that we must keep in mind. First, the measurements are generally made with no filter, so that the actual $Af\rho$ related to the red Johnson filter of our images, which we try to model, may differ somewhat to those shown in Figure 10, and also these differences might be time-variable. Second, a more important concern is that $Af\rho$ depends on the radius of the aperture used, unless the brightness dependence of the coma on the radius become ρ^{-1}. We have computed $Af\rho$ from the reduced images shown in Figure 1, at several aperture radii, from the brightness profiles. In Table 7 we show these measurements, along with some measurements by the association *Cometas-Obs* that are close in time to ours. The measurements by this group are made through a square $10''\times10''$ aperture that corresponds to the same area of a circular aperture of $5.64''$ in radius (21460 km in our images), so that they can be compared between them. As it is seen, our values are quite close to those reported by *Cometas-Obs* on the nights of July 23th and 24th. We also measured $Af\rho$ values for other apertures until an asymptotic, maximum value, is reached. These values are found to be a factor of 1.6-1.7 larger than the values reported with the $5.64''$ aperture. We will take this into account to make the constraints on $Af\rho$ values more flexible, i.e., allowing the model results to be up to a factor of 1.7 of the reported values of *Cometas-Obs* and *CARA*.

Since the reported measurements of $Af\rho$ by the amateur groups are taken at certain times that do not coincide with the time ranges defined by the model, in order to apply equation (9) we simply computed the average of the $Af\rho$ measurements contained in each time window as the value to fit in such time domain. We applied the model constraints to several hemispherical ejection and rotational nucleus models, specifically to the best fit model solutions shown in Tables 3 to 6.

The best fit hemispherical ejection model with $Af\rho$ constraints corresponds to model

run #136, for which we found σ=1.05×10^{-14}. Figure 11 displays the results of the model, and Figure 12 shows the comparison between measured and modeled $Af\rho$ values. It is remarkable that the model is in fact able to accommodate the different intensity outbursts of activity at the times they have been observed, as marked by arrows. The application of the $Af\rho$ constraints imply, as expected, an increase of σ over the unconstrained model, although the difference is not high. There is, however, a significant change in the size distribution power index, which with the $Af\rho$ constraints became $\langle\alpha\rangle$=–3.45±0.09. This change has been observed to occur in all cases when the $Af\rho$ constraints were applied to the best fit models of Table 3, so that they are all found to be within $\langle\alpha\rangle$=–3.5±0.1. Regarding the time-averaged dust mass loss, it is now 241 kg s^{-1}, which is lower than the unconstrained model result of 288 kg s^{-1}. For the remaining models of Table 3, the different time-averaged mass loss rates are all found to be in the range 300±100 kg s^{-1}, i.e., the same range obtained for the unconstrained solutions of Table 3.

The application of the $Af\rho$ constraints to the best fit rotational models (Tables 4 to 6) has limited the acceptable fits to those corresponding to a rotation period of P=15 days with C=3 only. Figure 13 shows the model results and Figure 14 shows the comparison between measured and modeled $Af\rho$ values, for the best fit model, which was found to be model #465 (see Table 6), with σ=6.2×10^{-15}. For this model, we obtained an average dust mass loss rate of 1100 kg s^{-1}, and a time average size distribution power index of $\langle\alpha\rangle$=–3.65±0.05. Similar values in both quantities are obtained for all the other cases having P=15 days with C=3, so that considering all of them we get $\langle\frac{dM}{dt}\rangle$=900±300 kg s^{-1}, and $\langle\alpha\rangle$=–3.6±0.1. There is a limitation in the number of $Af\rho$ constraints that could be applied because of shorter ejecta age compared to hemispherical ejection models, and the lack of measurements at 160 to 10 days preperihelion. There is considerable jumping in the modeled $Af\rho$ between 60 to 20 days before perihelion, sometimes reaching values as high as $Af\rho$=24000 cm, that contrast with all the other values measured. However, this might be not surprising if an outburst would have taken place on those dates, as some $Af\rho$ values as high as 16600 cm has been sometimes reported (e.g., Szabó et al. (2002)).

6. Conclusions

The Monte Carlo dust tail analysis of calibrated red images of comet 29P/Schwassmann-Wachmann 1 near the 2004 perihelion has given relevant information on the properties of the dust environment of the comet. We have considered two different approaches, one being the hemispherical ejection models and another the rotating nucleus models with active sources on the surface. Due to the outbursts that unevenly experience this comet we have in

principle not use any regularizing constraints for the solution of the overdetermined system of equations $\mathcal{AF} = \mathcal{I}$. In this scenario, we have come to the conclusion that a hemispherical ejection model give fits to the observed isophotes of a much less quality than the rotating nucleus models, mainly because of the observed coma asymmetry. Considering that the rotating 29P nucleus have rotation Euler angles as derived by Sekanina (1990), i.e., Φ=279°, and I=100°, we have shown that a model having a single active area of dust ejection on the southern hemisphere centered at ≈–30° latitude would be compatible with the observations, giving results far better than those given by the models with a fixed hemispherical cone with a sunward orientation. Our best fits for rotational nucleus models implies that the time-averaged particle size distribution function must be characterized by a power law with index –3.3±0.2, while the time-averaged mass loss rate is in the range 500-2000 kg s^{-1}, which confirms this object as likely the largest contributor to the interplanetary dust cloud (Fulle 1992). The large uncertainty in our results come from the fact that there are multiple solutions to the overdetermined system of equations giving similar fits to the observations, as detailed in Tables 4 to 6. Particularly, the rotation period is essentially not constrained, although slightly better results are obtained for a period of 15 days than for the shorter periods of 0.58 or 1.33 days, or for longer rotation periods such as 60 days.

The use of $Af\rho$(t) constraints on the system of equations that we have devised (equation 9) allowed us to better define the space of physical parameters parameters that would be compatible with the observed isophotes. Best fit hemispherical ejection models including those constraints gave an average dust mass loss rate of $\langle\frac{dM}{dt}\rangle$=300±100 kg s^{-1}, and a time-averaged power index of the size distribution function of $\langle\alpha\rangle$=–3.5±0.1. On the other hand, the application of the constraints to the rotational nucleus models has shown that the best fit correspond clearly to the those models having P=15 days, with a velocity constant of C=3, with gives $\langle\frac{dM}{dt}\rangle$=900±300 kg s^{-1}, and $\langle\alpha\rangle$=–3.6±0.1. These models would require the occurrence of an outburst 60 to 20 days preperihelion which we cannot validate because of lack of experimental data.

Finally, we must also point out that all the derived physical parameters for this comet on its dust environment are based on a series of images acquired in a particular time near its perihelion, so that a complete description of the cometary activity would require analysis of images acquired during a much longer time frame. Further work is underway with acquisition and analysis of a more complete data set.

We are indebted to an anonymous referee for his/her valuable comments and suggestions.

We are grateful to the Sierra Nevada Observatory staff, and the telescope operators Francisco J. Aceituno, Víctor Casanova, and Alfredo Sota for the image acquisition in service

mode.

The $Af\rho$ measurements were provided by both the Italian amateur association *CARA* Project, and the Spanish association *Cometas-Obs*. We are deeply indebted to Giannantonio Milani and Carlo Vinante from *CARA* and Julio Castellano and Esteban Reina from *Cometas-Obs* for providing us with those measurements.

This research was based on data obtained at the Observatorio de Sierra Nevada, which is operated by the Instituto de Astrofísica de Andalucía, CSIC.

This work was supported by contract AYA2007-63670, and by FEDER funds.

REFERENCES

A'Hearn, M. F., Schleicher, D.G., Feldman, P.D., Millis, R.L., and Thompson, D.T., 1984, AJ, 89, 579

Bartels, R.H., & Conn, A.R., 1980, ACM Transactions on Mathematical Software (TOMS), 6, 594

Burns, J.A., Lamy, P.L., & Soter, S. 1979, Icarus, 40, 1

Festou, M., Gunnarsson, M., Winnberg, A., Rickman, H., and Tancredi, G., 2001, Icarus, 150, 140

Finson, M., and Probstein, R., 1968, ApJ, 154, 327

Fulle, M. 1989, Astron. Astrophys., 217, 283

Fulle, M. 1992, Nature, 359, 42

Fulle, M. 1994, Astron. Astrophys., 282, 980

Fulle, M. 2000, Icarus 145, 239

Fulle, M. 2004, in Comets II, M. C. Festou, H. U. Keller, and H. A. Weaver (eds.), University of Arizona Press, Tucson, p. 565

Grün, E., Zook, H.A., Fechtig, H., and Giese, R.H., 1985, Icarus, 62, 244

Gunnarsson, M., Rickman, H., Festou, M.C., Winnberg, A., and Tancredi, G., 2002, Icarus, 157, 309

Gunnarsson, M., 2003, Astron. Astrophys., 398, 353

Hanner, M.S., & Newburn, R.L., 1989, AJ, 97, 254

Jewitt, D. 1990, ApJ, 351, 277

Jockers, K., Bonev, T., Ivanova, V., and Rauer, H., Astron. Astrophys., 260, 455

Jockers, K., Earth, Moon, and Planets, 79, 221

Meech, K., Belton, M., Mueller, B., Dicksion, M., and Heide, R., 1993, AJ, 106, 1222

Monet, D.G., et al., AJ, 125, 984

Moreno, F., Muñoz, O., Vilaplana, R., and Molina, A., 2003, ApJ, 595, 522

Moreno, F., Lara, L.M., Munõz, O., López-Moreno, J.J., and Molina, A., 2004, ApJ, 613, 1263

Mukai, T., 1986, Astron. Astrophys. 164, 397

Roemer, E. 1992, PASP, 70, 272

Sekanina, Z. 1981, Ann. Rev. Earth Planet. Sci., 9, 113

Sekanina, Z. 1990, AJ, 100, 1293

Senay, M.C. & Jewitt, D. 1994, Nature, 371 229

Stansberry, J. A., Van Cleve, J., Reach, W. T., Cruikshank, D. P., Emery, J. P., Fernandez, Y. R., Meadows, V. S., Su, K. Y. L., Misselt, K., Rieke, G. H., Young, E. T., Werner, M. W., Engelbracht, C. W., Gordon, K. D., Hines, D. C., Kelly, D. M., Morrison, J. E., and Muzerolle, J., 2004, ApJS, 154, 463

Sykes, M.V., & Walker, R.G., 1992, Icarus, 95, 180

Szabó, Gy.M., Kiss, L.L., Sárneczky, K., and Sziládi, K., 2002, Astron. Astrophys., 384, 702

Whipple, F.L.,1980, AJ, 85, 305

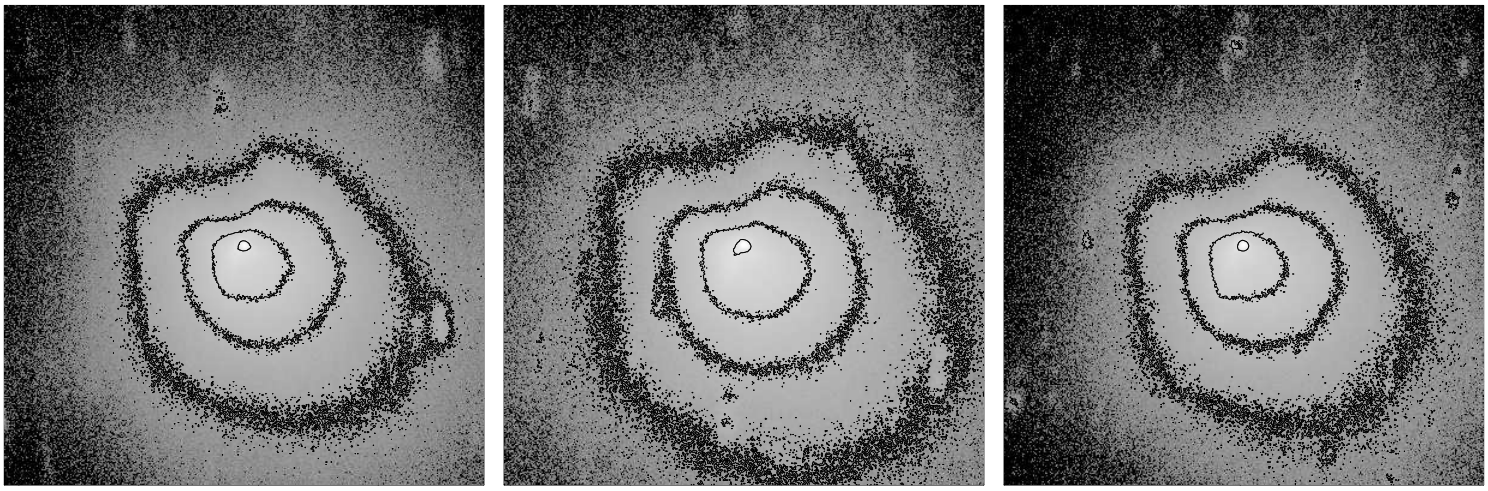

Fig. 1.— Calibrated images of comet 29P acquired on the Nasmyth focus of the 1.5 m telescope at Sierra Nevada Observatory through a Johnson red filter. Each image corresponds to the median of the images listed in Table 1, acquired on the nights of 23 (left), 24 (center), and 25 (right) July, 2004. The images cover an area of 400×400 pixel^2 ($\sim 3'\times3'$), or 706000^2 km^2. The contour levels correspond to 2×10^{-14}, 5×10^{-14}, 10^{-13}, and 3×10^{-13} solar disk intensity units. North is up, East to the left.

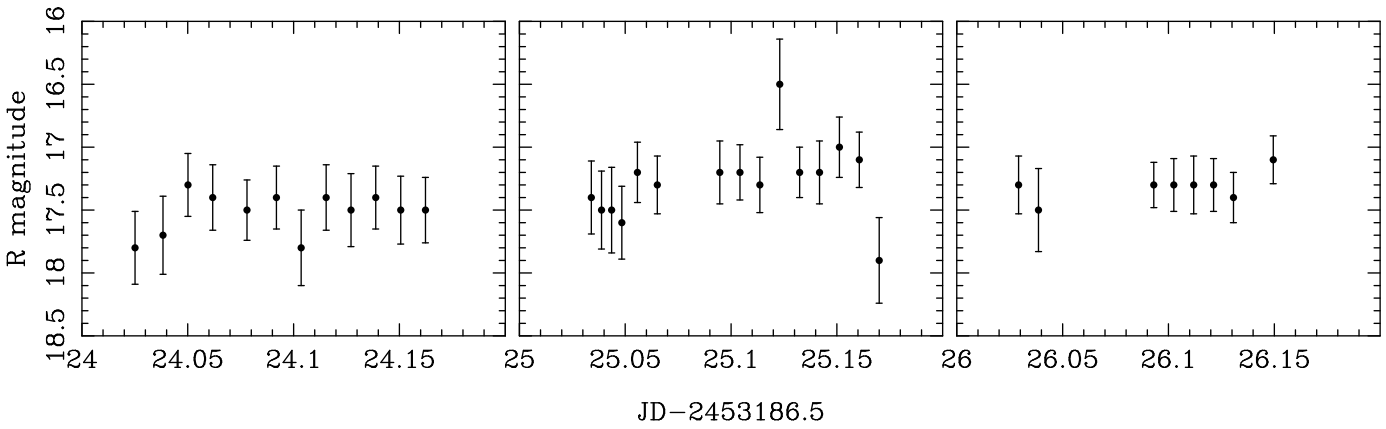

Fig. 2.— Light curve of 29P through a 4.6″ aperture from the individual images on each date (see Table 1). Left: Night of July 23, 2004; Center: July 24; Right: July 25.

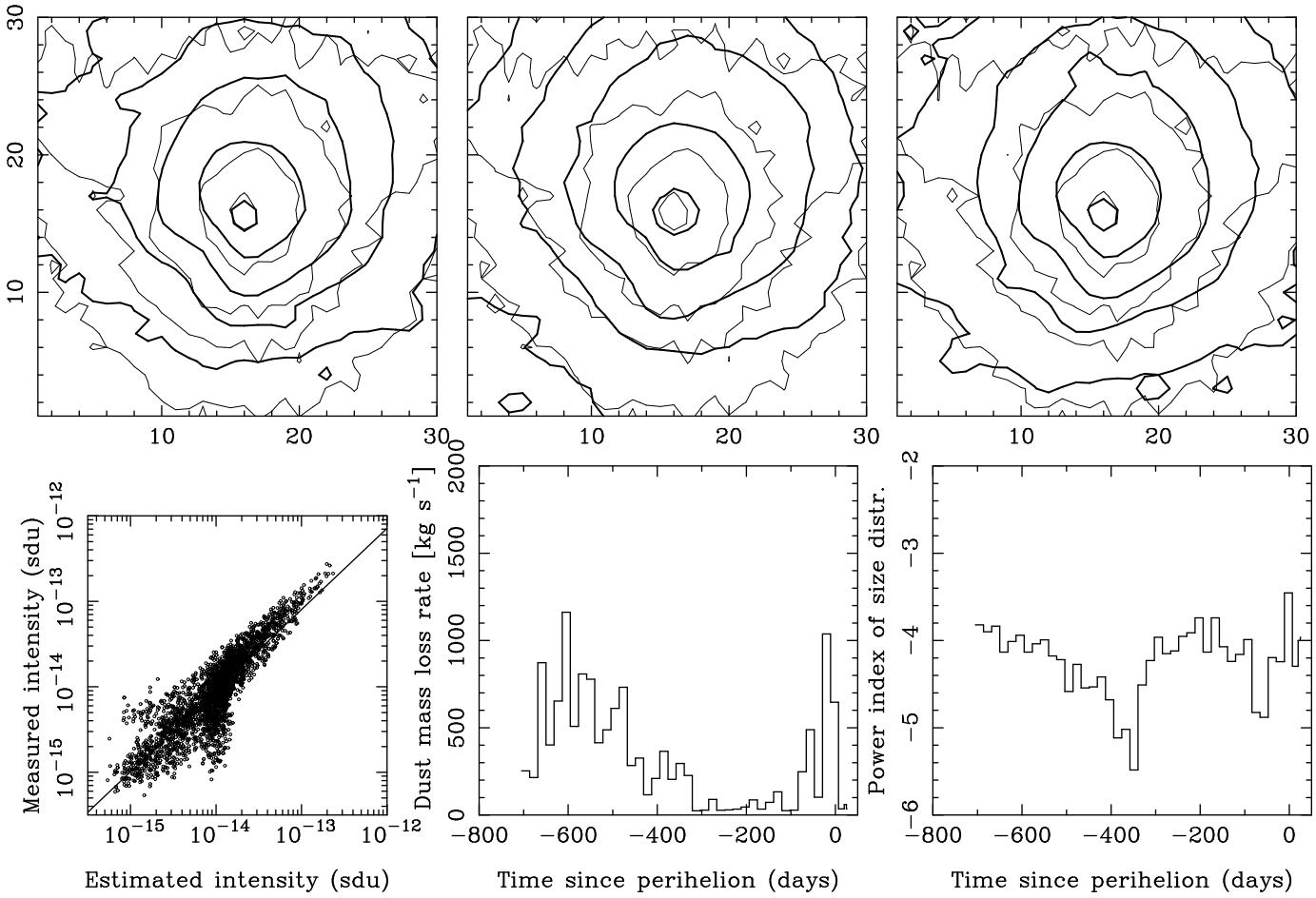

Fig. 3.— Results corresponding to run #303 for hemispherical ejection models. Upper three panels: observed (heavy solid lines) and modeled (thin lines) isophotes for the images on the nights of July 24 (upper left panel), 25 (upper central panel), and 26 (upper right panel) July, 2004. The contours correspond to 3×10^{-15}, 10^{-14}, 2×10^{-14}, 5×10^{-14}, and 1.5×10^{-13} solar disk intensity units. In the lower left panel, the correlation between the measured and modeled intensities is shown. The lower center panel shows the variation of the dust mass loss rate with time, while the lower right panel shows the variation of the time-averaged power index with time.

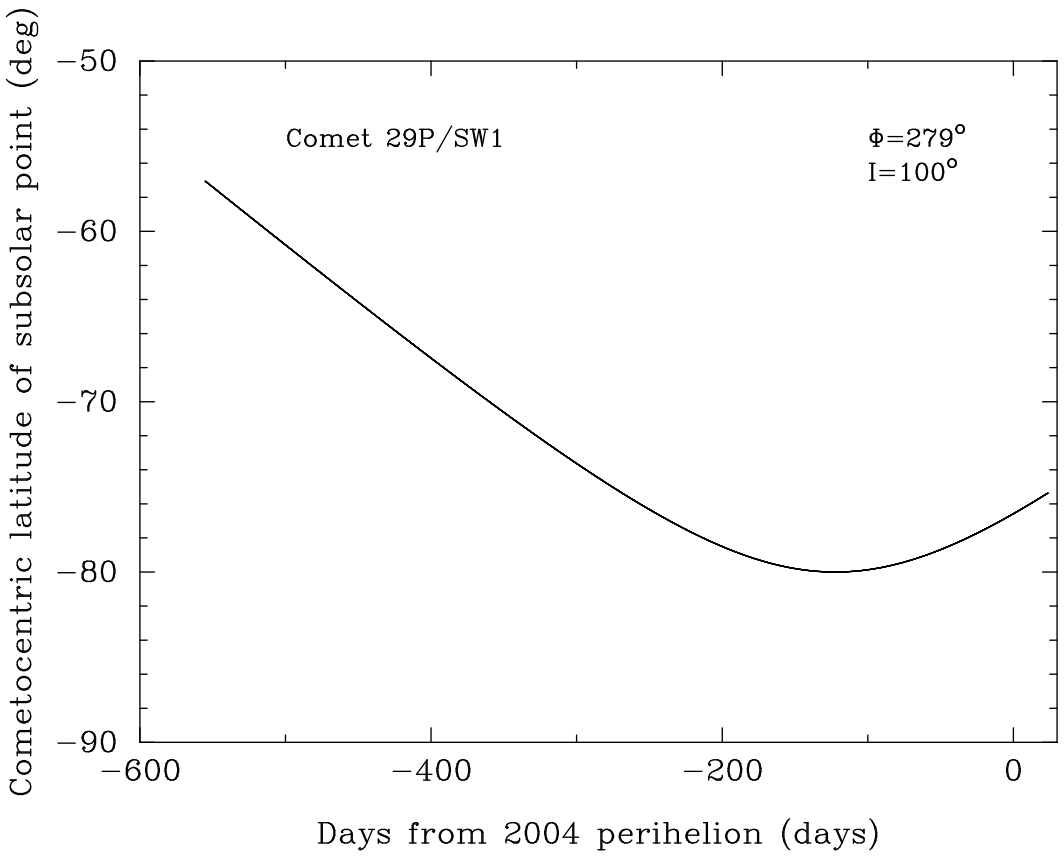

Fig. 4.— Cometocentric latitude of the subsolar point of comet 29P for rotational parameters Φ=279° and I=100° versus time.

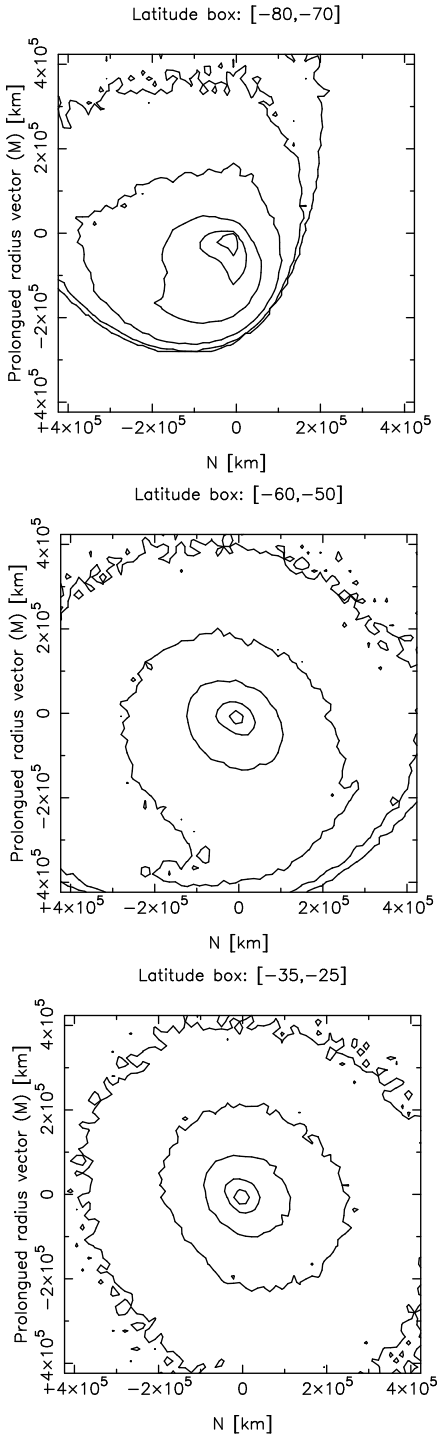

Fig. 5.— Contours plots in the (M,N) system (Finson and Probstein 1968) of the isophotes generated by a forward Monte Carlo calculation of the dust coma of 29P on July 24th, 2004, for rotational parameters Φ=279° and I=100° (Sekanina 1990), and a rotation period of 4.97 days (Whipple 1980). The ejecta is assumed to have an age of 115 days, and the ejected particles are distributed following a power-law size distribution function with exponent –1.5. The isophotes are spaced by 0.33 relative intensity units. The latitude boxes of the active areas are indicated on the top of each panel.

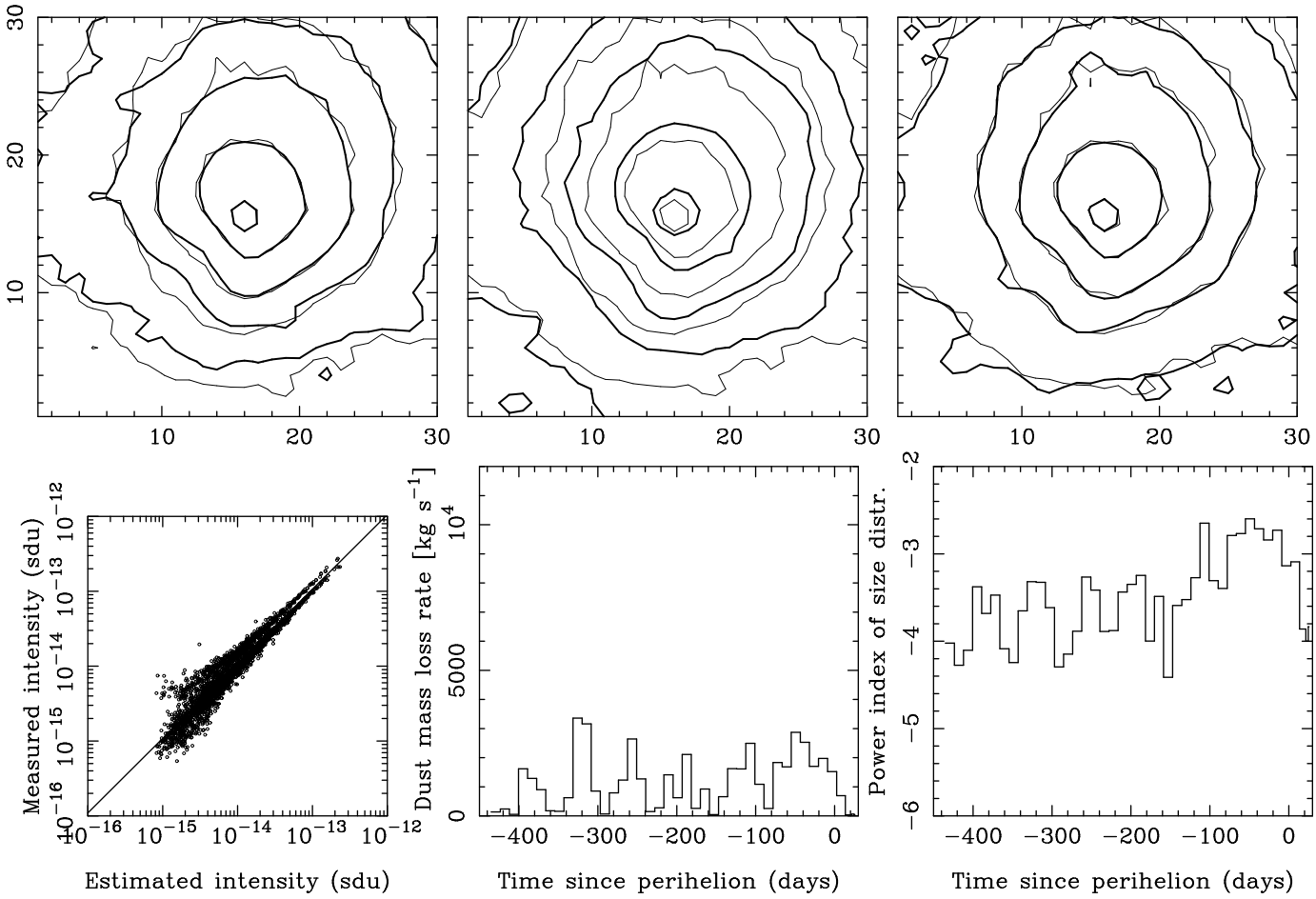

Fig. 6.— Results corresponding to run #328 for rotating nucleus models, corresponding to a rotation period of 0.58 days. Upper three panels: observed (heavy solid lines) and modeled (thin lines) isophotes for the images on the nights of July 24 (upper left panel), 25 (upper central panel), and 26 (upper right panel) July, 2004. The contours correspond to 3×10^{-15}, 10^{-14}, 2×10^{-14}, 5×10^{-14}, and 1.5×10^{-13} solar disk intensity units. In the lower left panel, the correlation between the measured and modeled intensities is shown. The lower center panel shows the variation of the dust mass loss rate with time, while the lower right panel shows the variation of the time-averaged power index with time.

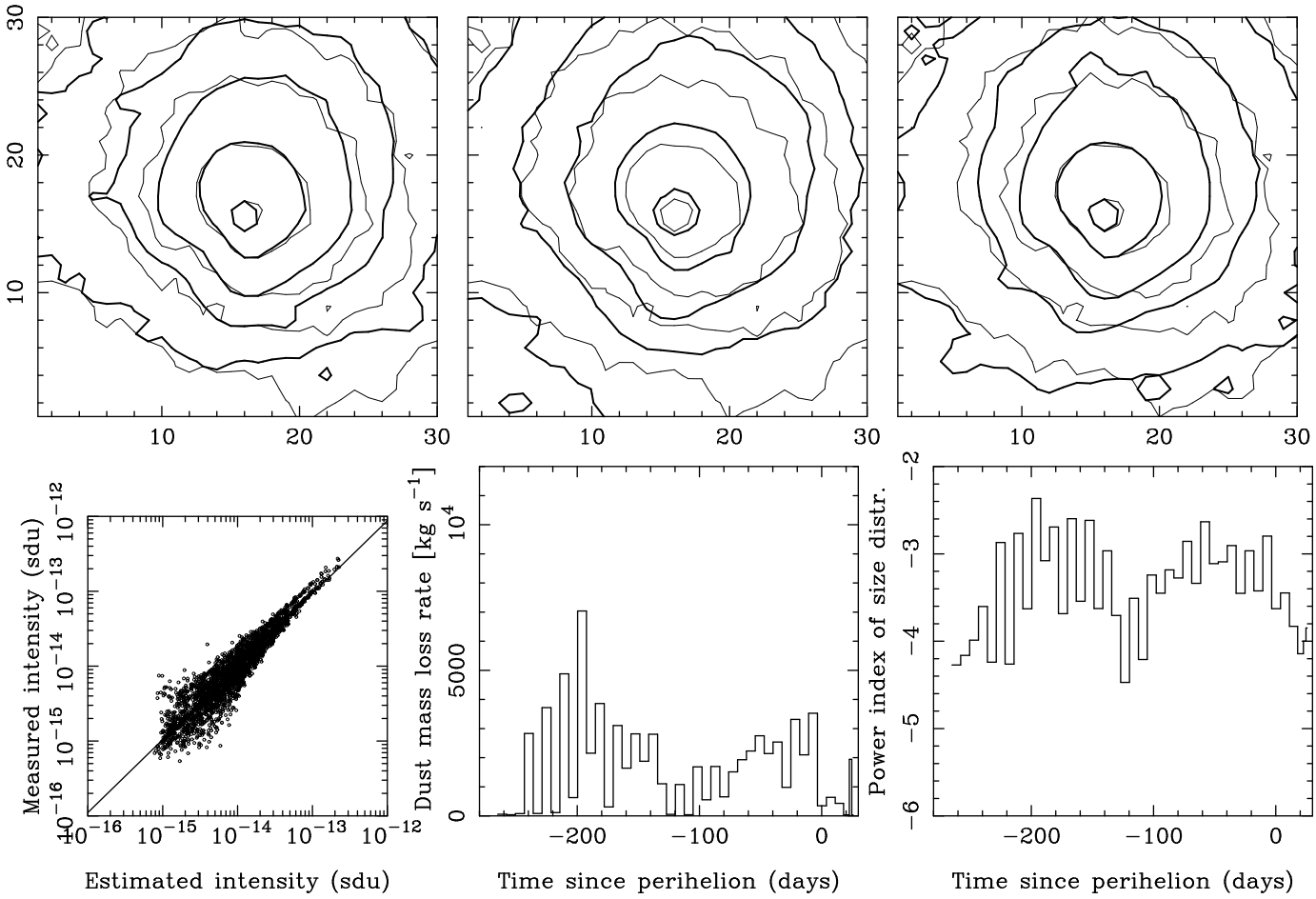

Fig. 7.— Results corresponding to run #902 for rotating nucleus models, corresponding to a rotation period of 1.33 days. Upper three panels: observed (heavy solid lines) and modeled (thin lines) isophotes for the images on the nights of July 24 (upper left panel), 25 (upper central panel), and 26 (upper right panel) July, 2004. The contours correspond to 3×10^{-15}, 10^{-14}, 2×10^{-14}, 5×10^{-14}, and 1.5×10^{-13} solar disk intensity units. In the lower left panel, the correlation between the measured and modeled intensities is shown. The lower center panel shows the variation of the dust mass loss rate with time, while the lower right panel shows the variation of the time-averaged power index with time.

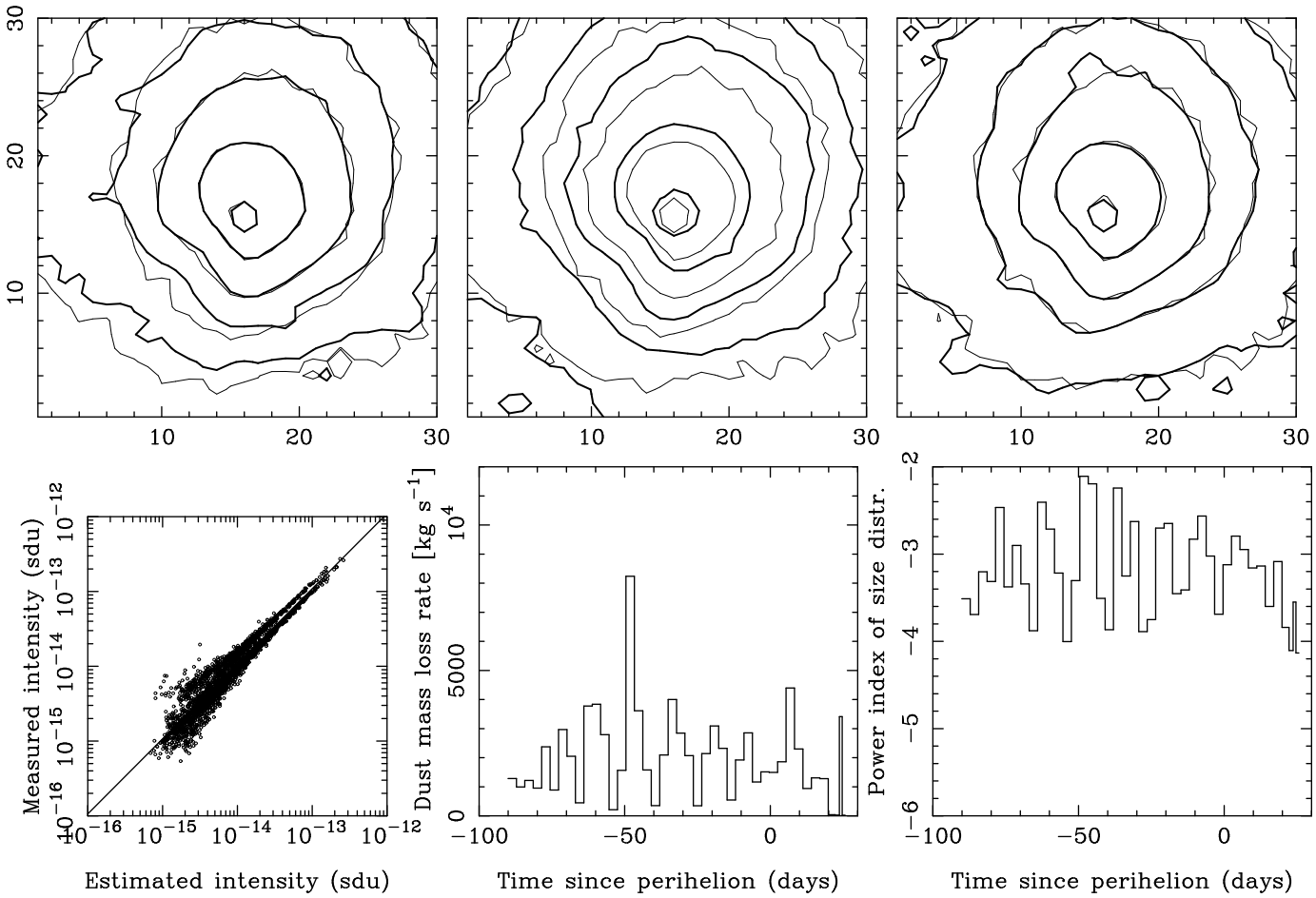

Fig. 8.— Results corresponding to run #2289 for rotating nucleus models, corresponding to a rotation period of 15 days, and a velocity constant C=5. Upper three panels: observed (heavy solid lines) and modeled (thin lines) isophotes for the images on the nights of July 24 (upper left panel), 25 (upper central panel), and 26 (upper right panel) July, 2004. The contours correspond to 3×10^{-15}, 10^{-14}, 2×10^{-14}, 5×10^{-14}, and 1.5×10^{-13} solar disk intensity units. In the lower left panel, the correlation between the measured and modeled intensities is shown. The lower center panel shows the variation of the dust mass loss rate with time, while the lower right panel shows the variation of the time-averaged power index with time.

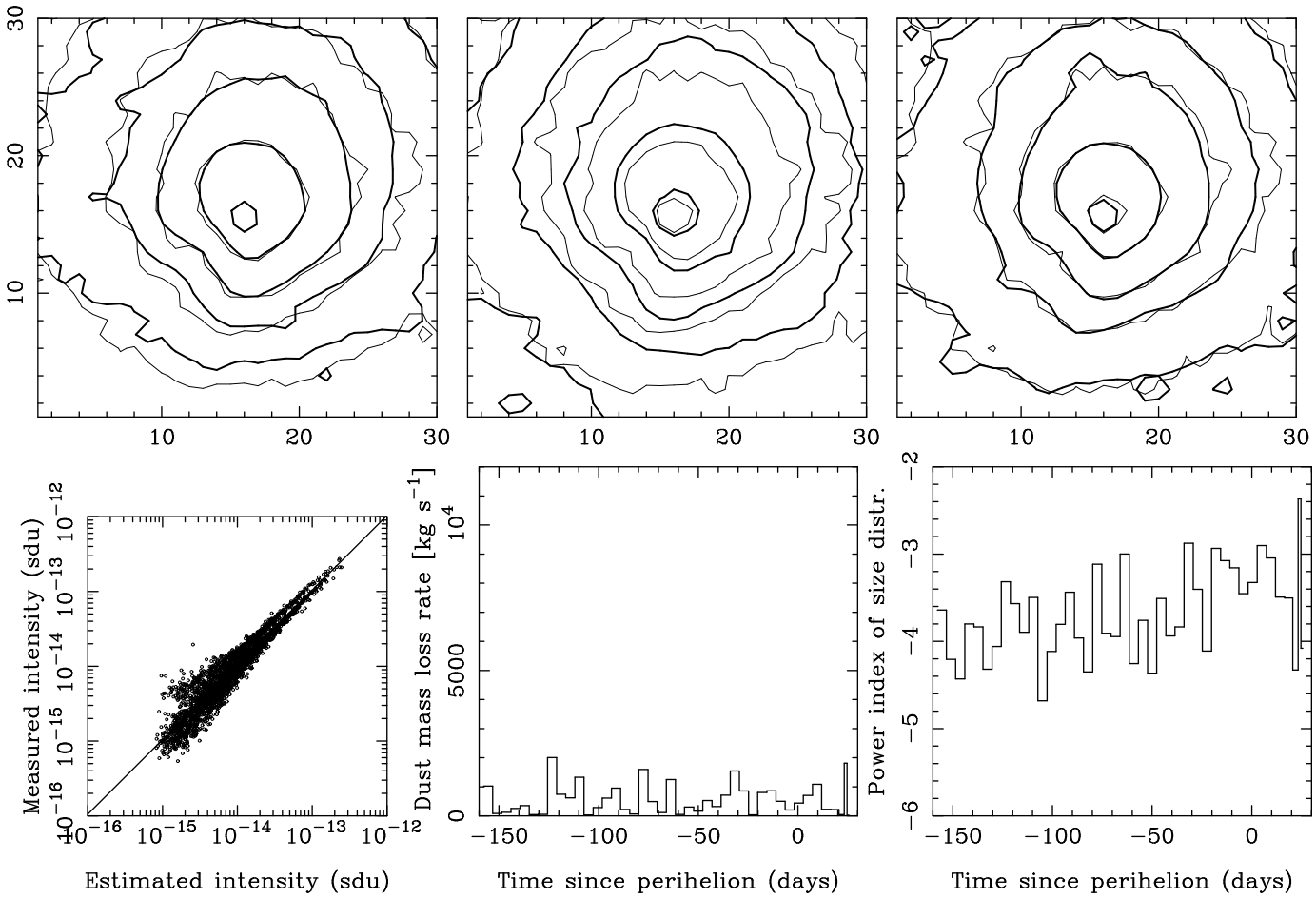

Fig. 9.— Results corresponding to run #3132 for rotating nucleus models, corresponding to a rotation period of 15 days, and a velocity constant C=3. Upper three panels: observed (heavy solid lines) and modeled (thin lines) isophotes for the images on the nights of July 24 (upper left panel), 25 (upper central panel), and 26 (upper right panel) July, 2004. The contours correspond to 3×10^{-15}, 10^{-14}, 2×10^{-14}, 5×10^{-14}, and 1.5×10^{-13} solar disk intensity units. In the lower left panel, the correlation between the measured and modeled intensities is shown. The lower center panel shows the variation of the dust mass loss rate with time, while the lower right panel shows the variation of the time-averaged power index with time.

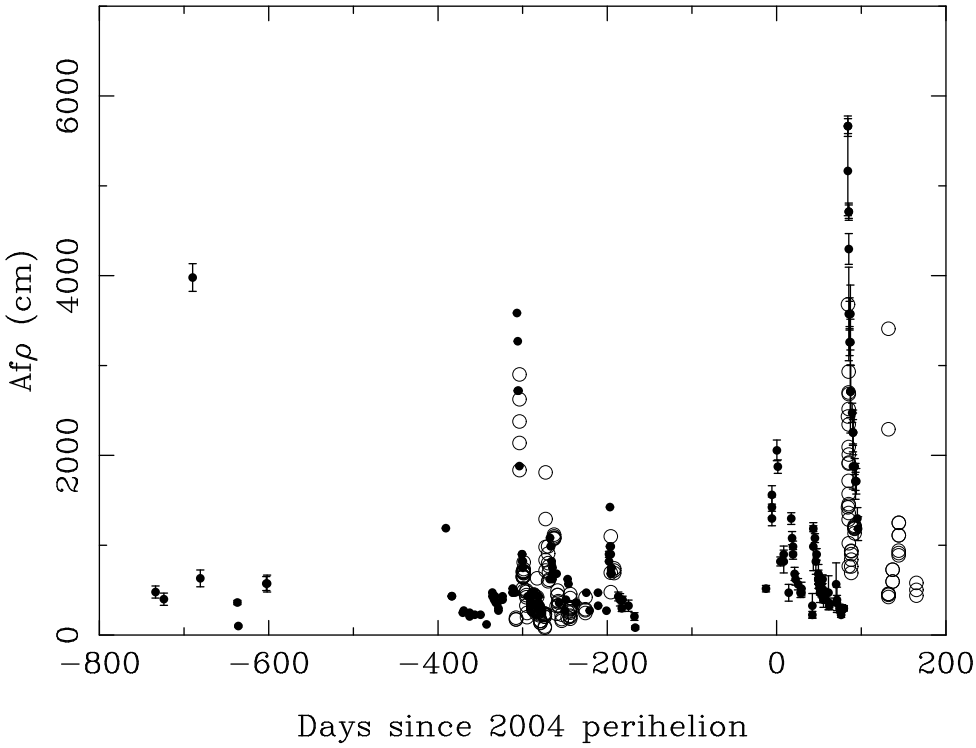

Fig. 10.— $Af\rho$ measurements as a function of time around the 2004 perihelion of 29P. The open circles correspond to the Italian *CARA* archive, while the solid circles come from the Spanish amateur association *Cometas-Obs*.

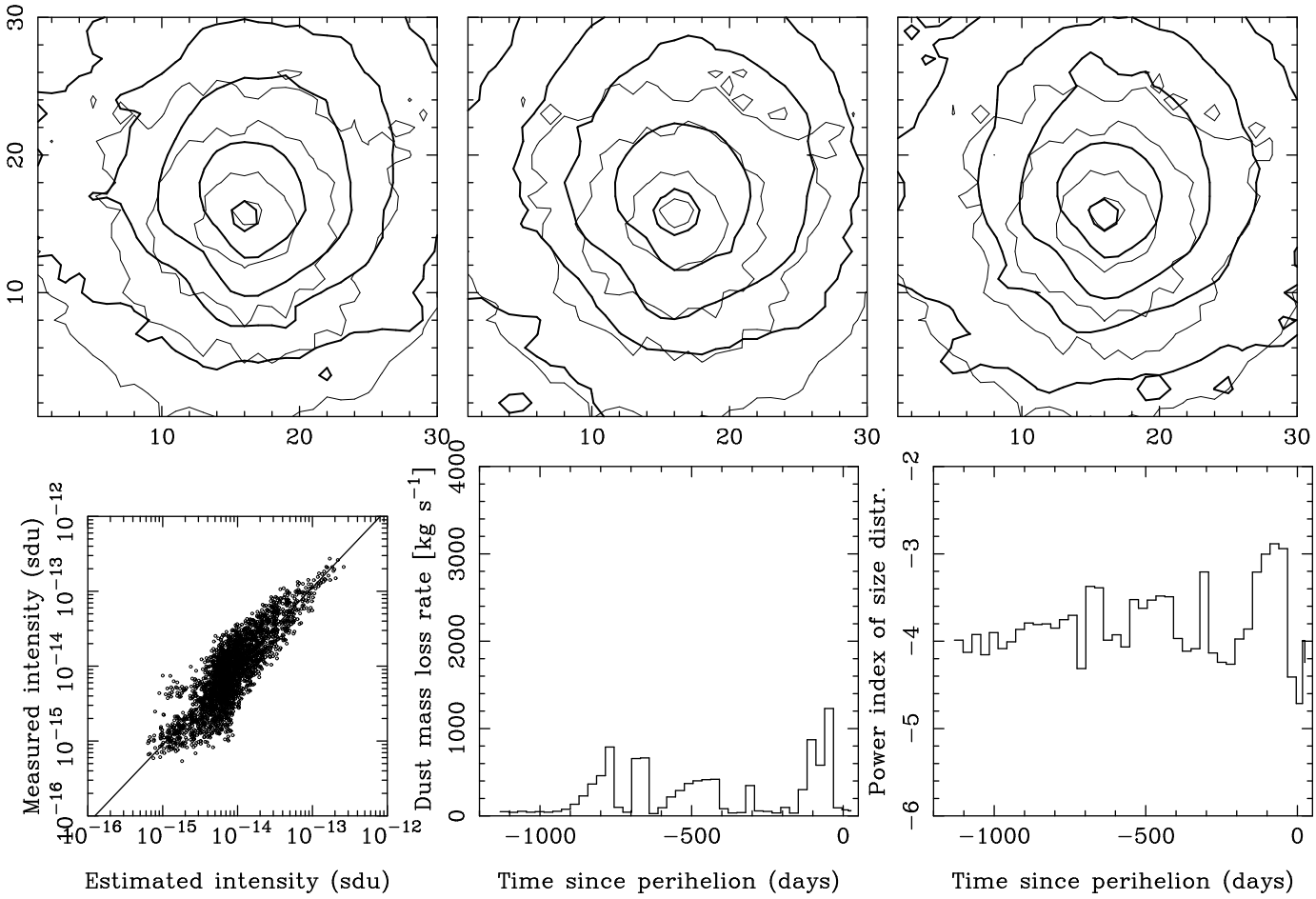

Fig. 11.— Results corresponding to run #136 for hemispherical ejection models, incorporating the $Af\rho$ constraints as given by equation 7. Upper three panels: observed (heavy solid lines) and modeled (thin lines) isophotes for the images on the nights of July 24 (upper left panel), 25 (upper central panel), and 26 (upper right panel) July, 2004. The contours correspond to 3×10^{-15}, 10^{-14}, 2×10^{-14}, 5×10^{-14}, and 1.5×10^{-13} solar disk intensity units. In the lower left panel, the correlation between the measured and modeled intensities is shown. The lower center panel shows the variation of the dust mass loss rate with time, while the lower right panel shows the variation of the time-averaged power index with time.

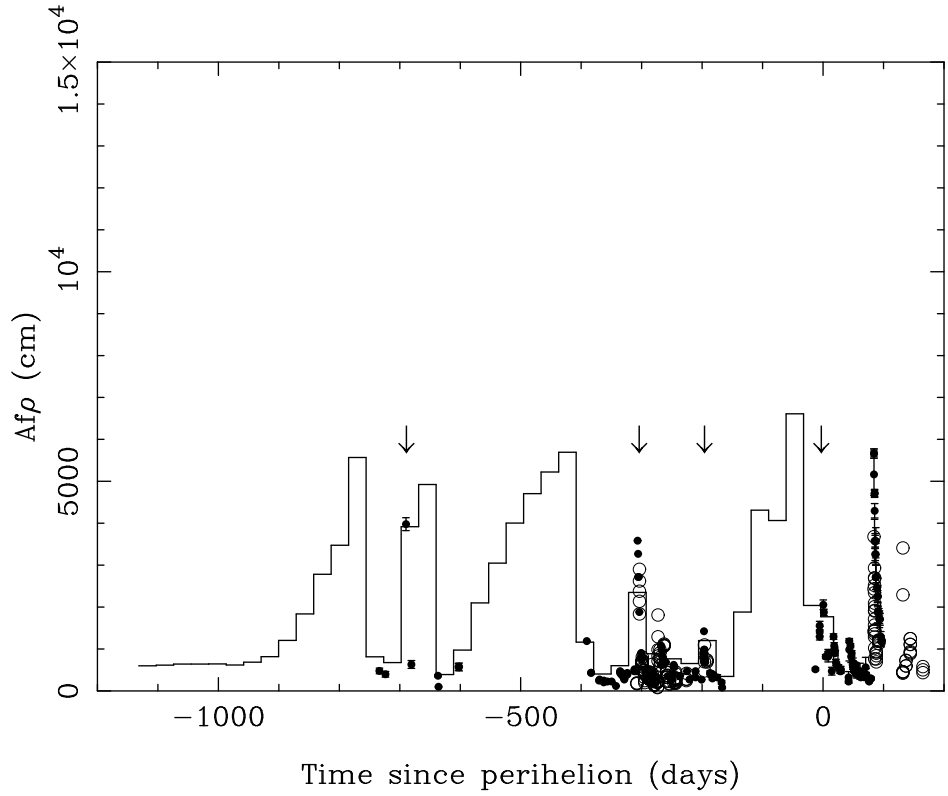

Fig. 12.— Measured $Af\rho$ by the Italian group *CARA* (open circles), and by the Spanish association *Cometas-Obs* (filled circles), along with the results of hemispherical ejection model #136 incorporating $Af\rho$ constraints as given by equation (9) (solid line).

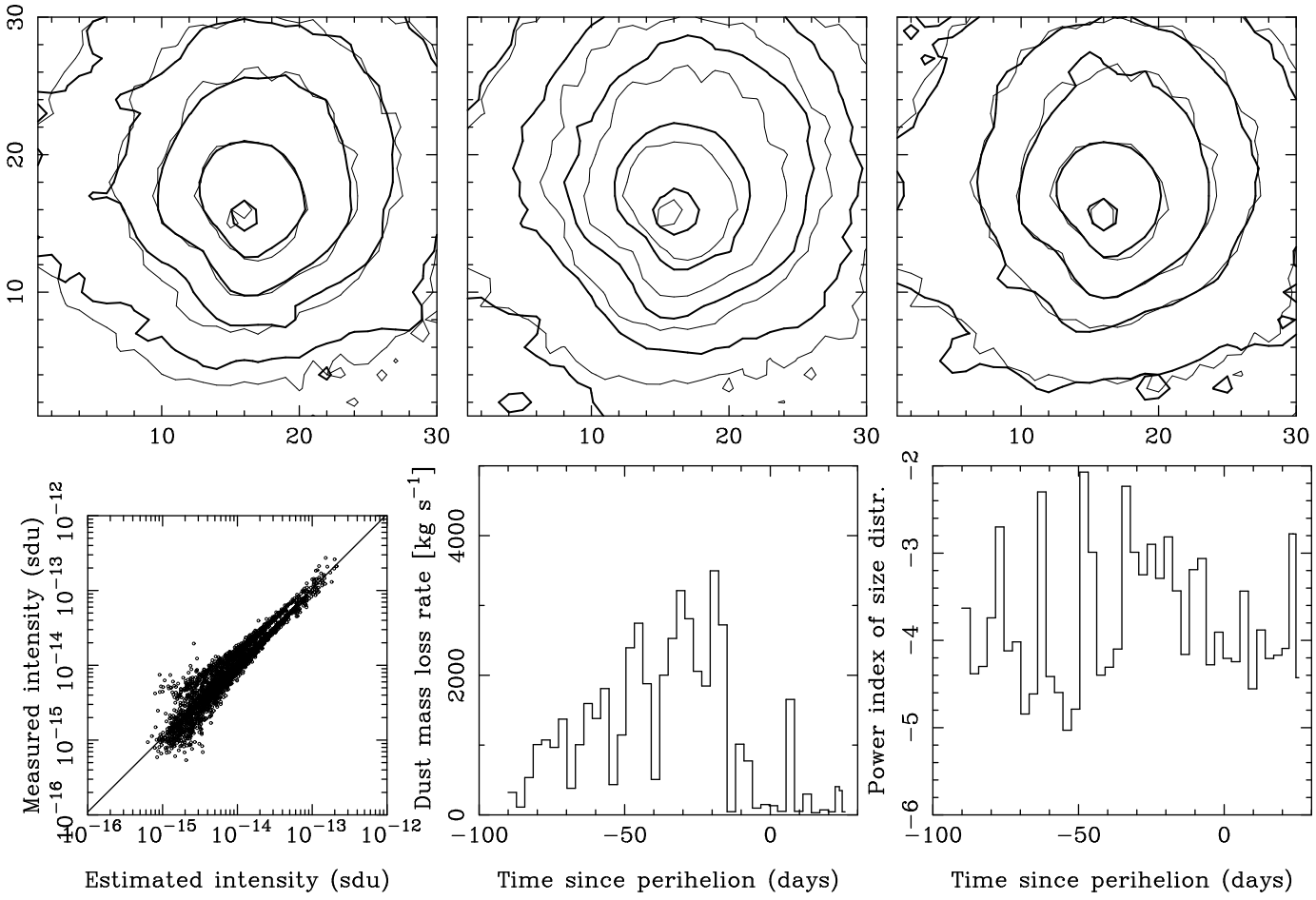

Fig. 13.— Results corresponding to run #465 for rotating nucleus models incorporating the $Af\rho$ constraints as given by equation (9). The model correspond to a rotation period of 15 days, and a velocity constant C=3. Upper three panels: observed (heavy solid lines) and modeled (thin lines) isophotes for the images on the nights of July 24 (upper left panel), 25 (upper central panel), and 26 (upper right panel) July, 2004. The contours correspond to 3×10^{-15}, 10^{-14}, 2×10^{-14}, 5×10^{-14}, and 1.5×10^{-13} solar disk intensity units. In the lower left panel, the correlation between the measured and modeled intensities is shown. The lower center panel shows the variation of the dust mass loss rate with time, while the lower right panel shows the variation of the time-averaged power index with time.

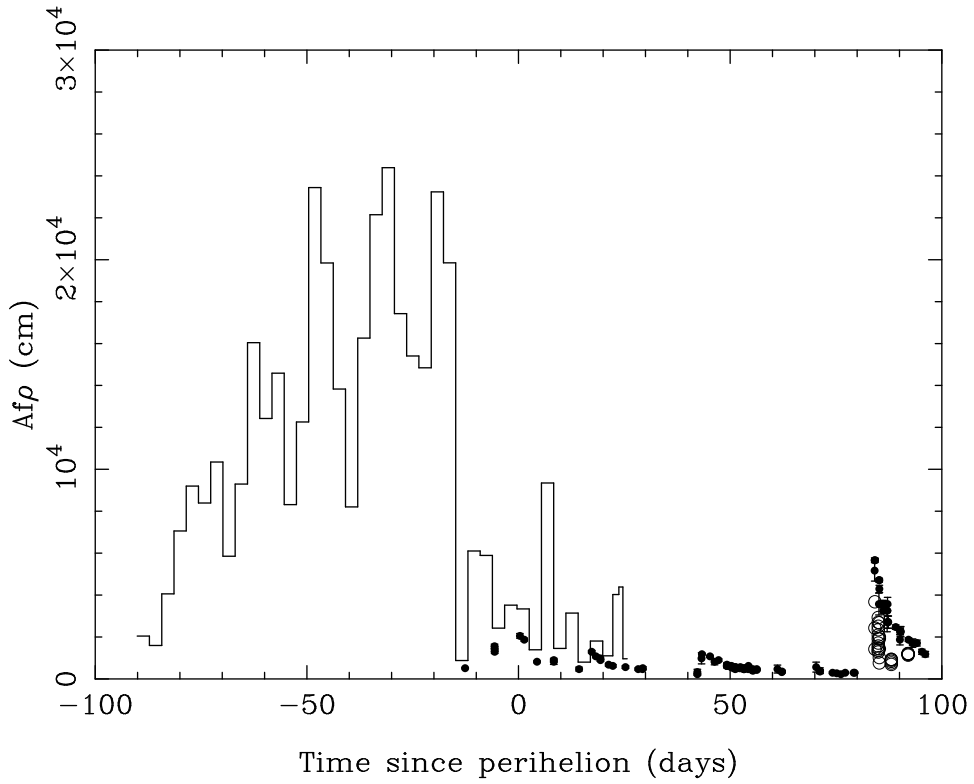

Fig. 14.— Measured $Af\rho$ by the Italian group *CARA* (open circles), and by the Spanish association *Cometas-Obs* (filled circles), along with the results of rotational nucleus model model #465 incorporating $Af\rho$ constraints as given by equation (9) (solid line).

Table 1. 29P/Schwassmann-Wachmann 1 Photometry.

2004 Date (UT) MM:DD hh:mm:ss	m_R (4.6 ″)	Mean Deviation	Number of stars	Seeing (″)
Jul 24 00 36 11	17.8	0.29	46	1.6
Jul 24 00 55 13	17.7	0.31	43	1.7
Jul 24 01 12 08	17.3	0.25	53	1.7
Jul 24 01 29 02	17.4	0.26	51	1.8
Jul 24 01 52 15	17.5	0.24	50	1.8
Jul 24 02 12 19	17.4	0.25	56	1.8
Jul 24 02 29 13	17.8	0.30	23	2.0
Jul 24 02 46 07	17.4	0.26	54	1.8
Jul 24 03 03 01	17.5	0.29	47	2.0
Jul 24 03 19 55	17.4	0.25	55	2.0
Jul 24 03 36 49	17.5	0.27	49	1.9
Jul 24 03 53 42	17.5	0.26	50	2.1
Jul 25 00 49 00	17.4	0.29	37	1.6
Jul 25 00 55 54	17.5	0.31	36	1.8
Jul 25 01 02 49	17.5	0.34	36	1.8
Jul 25 01 09 43	17.6	0.29	42	1.7
Jul 25 01 20 22	17.2	0.24	54	1.8
Jul 25 01 33 56	17.3	0.23	48	1.8
Jul 25 02 16 26	17.2	0.25	47	1.9
Jul 25 02 30 00	17.2	0.22	53	1.8
Jul 25 02 43 33	17.3	0.22	61	1.8
Jul 25 02 57 06	16.5	0.36	20	1.5
Jul 25 03 10 39	17.2	0.20	56	1.8
Jul 25 03 24 13	17.2	0.25	60	1.9
Jul 25 03 37 46	17.0	0.24	60	1.7
Jul 25 03 51 19	17.1	0.22	62	1.5
Jul 25 04 04 52	17.9	0.34	43	1.5
Jul 26 00 42 02	17.3	0.23	44	2.0
Jul 26 00 55 35	17.5	0.33	37	2.1
Jul 26 02 14 01	17.3	0.18	57	1.7

Table 1—Continued

2004 Date (UT) MM:DD hh:mm:ss	m_R (4.6 ″)	Mean Deviation	Number of stars	Seeing (″)
Jul 26 02 27 34	17.3	0.21	56	1.8
Jul 26 02 41 07	17.3	0.23	57	1.7
Jul 26 02 54 40	17.3	0.21	55	1.7
Jul 26 03 08 13	17.4	0.20	54	1.8
Jul 26 03 35 19	17.1	0.19	59	1.9

Table 2. Trial values of physical parameters of 29P for modeling.

Parameter	Value (or range of variation: start, end, step)
Integration times:	τ_1=0 s; log(τ_2)=6.6, 8.0, 0.2 (τ_2 in seconds)
$(1-\mu)_1$ limits:	log[$(1-\mu)_1$]=–5, –4, 0.25
$(1-\mu)_2$ limits:	log[$(1-\mu)_2$]=–2, 0, 0.25
Ejection velocity constant C:	C=1, 5, 2
Active area latitude range:	–35° to –25°
Obliquity:	I=100° (adopted from Sekanina (1990))
Argument of subsolar meridian at perihelion:	Φ=279° (adopted from Sekanina (1990))
Rotation period:	Assumed values: 14 hr, 32 hr, and 15 days

Table 3. Best fit model parameters and derived quantities for hemispherical ejection models.

# Run	log τ_2 (s)	log $(1-\mu)_1$	log $(1-\mu)_2$	C	σ (10^{-14} sdu)	$\langle \frac{dM}{dt} \rangle$ (kg s^{-1})	$\langle \alpha \rangle$
303	7.8	–4.75	–1.25	3	0.759	315	–4.4±0.1
735	7.8	–4.25	–1.25	3	0.764	330	–4.4±0.1
952	8.0	–4.00	–1.25	3	0.787	393	–3.8±0.2
783	7.8	–4.25	–0.75	3	0.809	230	–4.0±0.2
327	7.8	–4.75	–1.00	3	0.809	321	–4.1±0.2
759	7.8	–4.25	–1.00	3	0.810	273	–4.2±0.2
136	8.0	–5.00	–0.75	3	0.811	288	–3.7±0.2
87	7.8	–5.00	–1.25	3	0.812	353	–4.3±0.2
712	8.0	–4.25	–1.50	3	0.813	395	–4.4±0.2
590	7.6	–4.50	–0.50	3	0.813	190	–4.2±0.1

Table 4. Best fit model parameters and derived quantities for rotational nucleus models with P=0.58 days.

# Run	log τ_2 (s)	log $(1-\mu)_1$	log $(1-\mu)_2$	C	σ (10^{-14} sdu)	$\langle \frac{dM}{dt} \rangle$ (kg s^{-1})	$\langle \alpha \rangle$
328	7.6	–5.00	–1.00	3	0.509	1120	–3.27±0.08
976	7.6	–4.75	–1.00	3	0.509	1118	–3.36±0.08
118	8.0	–5.00	–1.75	3	0.509	2229	–3.16± 0.07
1624	7.6	–4.50	–1.00	3	0.511	1140	–3.23±0.08
2272	7.6	–4.25	–1.00	3	0.512	1084	–3.28±0.07
208	7.6	–5.00	–1.50	5	0.513	3497	–2.90±0.07
694	8.0	–4.75	–2.00	3	0.513	2826	–3.12±0.07
46	8.0	–5.00	–2.00	3	0.513	2216	–3.15±0.08
2800	7.6	–4.00	–1.50	5	0.514	2879	–2.88±0.09
904	7.6	–4.75	–1.25	3	0.514	1605	–3.19±0.06

Table 5. Best fit model parameters and derived quantities for rotational nucleus models with P=1.33 days.

# Run	log τ_2 (s)	log $(1-\mu)_1$	log $(1-\mu)_2$	C	σ (10^{-14} sdu)	$\langle \frac{dM}{dt} \rangle$ (kg s^{-1})	$\langle \alpha \rangle$
902	7.4	–4.75	–1.25	3	0.530	1699	–3.02±0.08
182	7.4	–5.00	–1.50	3	0.532	2120	–3.29±0.06
1478	7.4	–4.50	–1.50	3	0.533	2008	–3.30±0.06
2198	7.4	–4.25	–1.25	3	0.535	1890	–3.00±0.08
710	7.4	–4.75	–2.00	5	0.536	5652	–3.35±0.06
2126	7.4	–4.25	–1.50	3	0.537	1925	–3.30±0.06
1550	7.4	–4.50	–1.25	3	0.538	1680	–3.08±0.07
38	7.4	–5.00	–2.00	3	0.539	3444	–3.77±0.05
62	7.4	–5.00	–2.00	5	0.539	5440	–3.48±0.05
254	7.4	–5.00	–1.25	3	0.539	1475	–3.16±0.08

Table 6. Best fit model parameters and derived quantities for rotational nucleus models for P=15 days.

# Run	log τ_2 (s)	log $(1-\mu)_1$	log $(1-\mu)_2$	C	σ (10^{-14} sdu)	$\langle \frac{dM}{dt} \rangle$ (kg s^{-1})	$\langle \alpha \rangle$
2289	7.0	–4.25	–1.00	5	0.493	1980	–3.14±0.06
2937	7.0	–4.00	–1.00	5	0.495	2138	–3.10±0.06
345	7.0	–5.00	–1.00	5	0.496	2081	–3.15±0.06
465	7.0	–5.00	–0.50	3	0.496	692	–3.17±0.05
2286	6.8	–4.25	–1.00	5	0.496	1947	–3.45±0.05
3132	7.2	–4.00	–0.25	3	0.497	564	–3.46±0.07
2934	6.8	–4.00	–1.00	5	0.497	1998	–3.43±0.06
1113	7.0	–4.75	–0.50	3	0.497	661	–3.20±0.05
2865	7.0	–4.00	–1.25	5	0.497	2206	–3.37±0.07
342	6.8	–5.00	–1.00	5	0.498	1990	–3.47±0.05
993	7.0	–4.75	–1.00	5	0.498	2042	–3.16±0.06
3057	7.0	–4.00	–0.50	3	0.498	689	–3.20±0.04

Table 7. Comparison of measurements of $Af\rho$ [cm] on the different nights.

Source	2004/07/23	2004/07/24	2004/07/25
This work (Ap. radius=5.6″)	503	611	461
This work (Max. value)	809	1075	810
Cometas-Obs (10″×10″)[a]	471±54		
Cometas-Obs (10″×10″)[b]		471±48	
Cometas-Obs (10″×10″)[c]		516±72	

[a]Observation date: 2004/07/24 00:03 UT

[b]Observation date: 2004/07/25 01:13 UT

[c]Observation date: 2004/07/25 02:26 UT